






# TiN nanobridge Josephson junctions and nanoSQUIDs on SiN-buffered Si

M I Faley<sup>1,4,\*</sup> , H Fiadziushkin<sup>2</sup> , B Frohn<sup>3</sup> , P Schüffelgen<sup>3</sup>   
and R E Dunin-Borkowski<sup>1,4</sup> 

<sup>1</sup> Peter Grünberg Institute 5, Forschungszentrum Jülich GmbH, 52425 Jülich, Germany

<sup>2</sup> Faculty of Electrical Engineering and Information Technology, RWTH Aachen University, 52062 Aachen, Germany

<sup>3</sup> Peter Grünberg Institute 9, Forschungszentrum Jülich GmbH, 52425 Jülich, Germany

<sup>4</sup> Ernst Ruska-Centre for Microscopy and Spectroscopy with Electrons, Forschungszentrum Jülich GmbH, 52425 Jülich, Germany

E-mail: [m.faley@fz-juelich.de](mailto:m.faley@fz-juelich.de)

Received 26 December 2021, revised 30 March 2022

Accepted for publication 6 April 2022

Published 20 April 2022



CrossMark

## Abstract

We report the fabrication and properties of titanium nitride (TiN) nanobridge Josephson junctions (nJJs) and nanoscale superconducting quantum interference devices (nanoSQUIDs) on SiN-buffered Si substrates. The superior corrosion resistance, large coherence length, suitable superconducting transition temperature and highly selective reactive ion etching (RIE) of TiN compared to e-beam resists and the SiN buffer layer allow for reproducible preparation and result in long-term stability of the TiN nJJs. High-resolution transmission electron microscopy reveals a columnar structure of the TiN film on an amorphous SiN buffer layer. High-resolution scanning electron microscopy reveals the variable thickness shape of the nJJs. A combination of wet etching in 20% potassium hydroxide and RIE is used for bulk nanomachining of nanoSQUID cantilevers. More than 20 oscillations of the  $V(B)$  dependence of the nanoSQUIDs with a period of  $\sim 6$  mT and hysteresis-free  $I(V)$  characteristics (CVCs) of the all-TiN nJJs are observed at 4.2 K. CVCs of the low- $I_c$  all-TiN nJJs follow theoretical predictions for dirty superconductors down to  $\sim 10$  mK, with the critical current saturated below  $\sim 0.6$  K. These results pave the way for superconducting electronics based on nJJs operating non-hysteretically at 4.2 K, as well as for all-TiN qubits operating at sub-100 mK temperatures.

Keywords: titanium nitride, nanobridge, Josephson junction, nanoSQUID

(Some figures may appear in colour only in the online journal)

## 1. Introduction

Superconducting quantum interference devices (SQUIDs) play a pivotal role in many applications [1–5]. The versatility of SQUIDs is accompanied by high demand on their design

optimization to achieve the most sensitive detection of magnetic flux for a specific application. The magnetic fields of nanometer-scale magnetic objects may contain high spatial frequency components that impose requirements on the spatial resolution of a SQUID. The lateral dimensions of the SQUID loop may then need to be  $< 1 \mu\text{m}$  (nanoSQUID), with the nanoSQUID placed at a distance of less than 100 nm from the object [6–8]. Recent research has included studies of the magnetization dynamics of nanometer-scale magnetic objects [9], with nanoSQUIDs serving as detectors with single spin magnetic dipole sensitivity, a spatial resolution down to the nanometer scale and operation up to THz frequencies.

\* Author to whom any correspondence should be addressed.



Original content from this work may be used under the terms of the [Creative Commons Attribution 4.0 licence](https://creativecommons.org/licenses/by/4.0/). Any further distribution of this work must maintain attribution to the author(s) and the title of the work, journal citation and DOI.

State-of-the-art microwave SQUIDs are able to operate at frequencies of up to  $\sim 10$  GHz [10]. NanoSQUIDs that are based on nanobridge Josephson junctions (nJJs) require only single-layer technology and should have better temporal resolution, as a result of the negligible capacitance of the nanobridges of  $\sim 0.01$  fF [11], when compared to the capacitances of three-layer tunnel Josephson junctions of  $>20$  fF [12].

Further miniaturization of nanoSQUIDs and other superconducting circuits requires a paradigm shift in the design and fabrication of Josephson junctions from three-layer structures to much smaller nJJs, whose size is limited only by the resolution of single-layer patterning technology. A further advantage of nJJs is that they are able to conduct the highest possible critical current density  $J_c$ , which is necessary to provide an optimal SQUID parameter  $\beta_L = 2LI_c/\Phi_0 \cong 1$ , where  $L$  is the geometrical inductance of the nanoSQUID loop,  $\Phi_0 = h/2e \cong 2.068$  fT m<sup>2</sup> is a magnetic flux quantum and the critical current  $I_c = J_c \times \sigma$ , where  $\sigma$  is the cross-sectional area of the nJJs. Achievable values of  $J_c$  in nJJs approach the critical current density of the constituent superconducting films, which is, for example,  $\sim 30$  MA cm<sup>-2</sup> for Nb thin films [13].

Single layer ‘planar’ nanoSQUIDs with nJJs have been realized by different nanopatterning methods on conventional planar substrates using different superconducting materials, including Nb [14–16], NbN [17, 18], MoRe [19], YBa<sub>2</sub>Cu<sub>3</sub>O<sub>7-x</sub> (YBCO) [20–22], Al [23] and titanium nitride (TiN) [24].

The Josephson effect in nJJs can be explained qualitatively within Ginzburg–Landau theory for nJJs whose length is much smaller than the superconducting coherence length (see [24] and references therein). The  $I(V)$  characteristics (CVCs) of nJJs and nanoSQUIDs with nJJs can exhibit hysteretic behavior as a result of (a) overheating hysteresis of the nJJs [19], or (b) multivalued current-phase characteristics  $I(\varphi)$  of the nJJs and related phase slippage in the nJJs, as suggested in [11]. Thermal hysteresis originates from heating and the transition of nJJs to the normal state and is usually observed for nJJs with critical currents  $I_c > 20$   $\mu$ A [11, 19]. The critical currents of nJJs can be reduced in a controlled way by ion beam etching [17], but the spread of critical currents of nJJs increases when their thickness and/or width become comparable to the grain size in a usually polycrystalline superconducting film of nJJs.

An increase in the length of an nJJ can lead to a deviation from ideal Josephson behavior  $I(\varphi) \sim \sin(\varphi)$  and, at values greater than 3.5 times the coherence length  $\xi$ , the  $I(\varphi)$  characteristics can then become multivalued [25]. In Nb, NbN and MoRe thin films,  $\xi(0$  K) is  $\sim 10$  nm and the superconducting transition temperature  $T_c \gg 4.2$  K. The short coherence length in these materials and the much shorter coherence length in the high- $T_c$  superconductor YBCO leads to large upper critical magnetic fields and is advantageous for high field applications, such as the investigation of magnetic nanoparticles (see, for example [17]). However, this requires the use of sophisticated patterning techniques with sub-10 nm spatial resolution to provide non-hysteretic operation of the nanoSQUID at 4.2 K [8, 16] or 50 K [20]. This restriction is lifted within an operating temperature range of  $7$  K  $< T < T_c$  [26], within which the absence of hysteresis in CVCs can be

explained by an increase in the superconducting coherence length in Nb  $\xi \propto 1/\sqrt{1 - T/T_c}$  at a temperature  $T$  of the nJJs that is in the vicinity of  $T_c$ , according to Ginzburg–Landau theory [27]. Thin films of TiN have  $T_c$  values of between 4.3 and 4.8 K and a coherence length  $\xi(4.2$  K)  $> 100$  nm [24], resulting in much easier realization of hysteresis-free operation of TiN nJJs at 4.2 K.

The superior corrosion resistance of TiN [28] is advantageous for the long-term stability of nJJs and nanoSQUIDs. TiN films improve the quality factors of resonators by up to  $10^7$  [29] and have fewer losses than Nb, Re or Al films [30]. In transmon qubits, the replacement of Al on TiN in shunting capacitors has led to a sixfold enhancement of relaxation and dephasing times [31]. A further enhancement of coherence was observed in all-nitride superconducting qubit heterostructures that were grown epitaxially on Si substrates with TiN buffer layers [32]. The realization of all-TiN qubits using nJJs in multilayer qubit technology would reduce dissipation, which is related to the presence of quantum two-level states (TLSs) in oxides, especially at interfaces [33]. The preparation of TiN nJJs on oxide-free substrates, such as Si substrates passivated/buffered by SiN layers, would be preferable, in order to avoid the need for Al<sub>2</sub>O<sub>3</sub> tunnel barriers in superconducting qubits and thus exclude such TLSs. Domain-matching epitaxy of TiN on Si substrates has been demonstrated in [34]. However, such TiN films are still polycrystalline [24]. TiN films prepared on pure Si have practically the same superconducting properties as TiN films grown on SiN-buffered Si, which are also free of oxygen, opening the possibility to realize all-TiN superconducting devices on SiN membranes for their use, for example, on samples in transmission electron microscopes.

In this paper, we report an investigation of nanoSQUIDs that are based on all-TiN nJJs, are manufactured on SiN-buffered Si substrates and are intended for operation at 4.2 K. The microstructures of the multilayers and devices are observed by high-resolution transmission electron microscopy (HRTEM) and high-resolution scanning electron microscopy (HRSEM). Current–voltage characteristics of the low- $I_c$  all-TiN nJJs are examined at different temperatures down to 9 mK. A process for the fabrication of SiN membranes by combining wet etching in 20% potassium hydroxide (KOH) and reactive ion etching (RIE) for the production of TiN-nanoSQUID cantilevers is also outlined.

## 2. Materials and methods

Pulsed reactive DC magnetron sputtering of a 99.95% pure TiN target of diameter 50 mm was used for the preparation of 100 nm thick films. Simultaneously, four samples were prepared on 10 mm  $\times$  10 mm  $\times$  0.4 mm Si (001) substrates, which were coated on both sides by low pressure chemical vapor deposited (LPCVD) 40 nm thick Si<sub>3</sub>N<sub>4</sub> (SiN) films. A few TiN films were prepared under the same conditions on MgO (001) substrates, in order to compare their epitaxial growth and superconducting properties. The substrates were cleaned in different solvents, rinsed in deionized water and etched using an Ar<sup>+</sup> ion beam under normal incidence to the

substrate surface to remove a few nanometers of SiN shortly before placement of the substrates in an in-house-assembled sputtering machine. In the sputtering machine, the substrates lay freely on a plate, whose temperature could be set between liquid nitrogen temperature (77.4 K) and a temperature of 920 °C obtained by using a THERMOCOAX heating element. The sputtering machine was pumped to a background pressure of less than  $10^{-7}$  mbar by using oil-free pumps. A gas mixture of 99.9999% pure Ar and N<sub>2</sub> in the ratio 9–1, respectively, at a total pressure of  $\sim 0.01$  mbar was used for deposition. The deposition rate of the TiN films was  $\sim 1$  nm min<sup>-1</sup> at a DC voltage bias of 250 V, a DC current of 100 mA and a heater temperature of 920 °C, which corresponds to a substrate temperature  $T_{\text{sub}}$  of  $\sim 800$  °C. The sputtering chamber was out-gassed during presputtering onto a closed shutter for more than 2 h prior to deposition on samples.

RIE and masks of AZ<sup>®</sup>nLOF2020 resist were used to pattern TiN films with a spatial resolution down to 10 nm. The resist was diluted by AZ<sup>®</sup>EBR solvent in the proportion one part nLOF2020 to three parts EBR for  $\sim 100$  nm thickness at a 4 krpm rotation speed of spin coating. A dose of 120  $\mu\text{C cm}^{-2}$  at an accelerating voltage of 100 kV was used for exposure of the resist. An Oxford Instruments PlasmaLab System 100 in the clean room of the Helmholtz Nano Facility (HNF) in Forschungszentrum Jülich was used to perform RIE of the TiN films in a pure SF<sub>6</sub> atmosphere at a pressure of 5 Pa and a power of the RF plasma of 25 W. After RIE, residuals of the resist were removed from the samples with a dip in acetone and propanol in an ultrasonic bath. Contact pads consisting of 20 nm Pt and 100 nm Ag films were deposited through a Ti shadow mask.

Of the four samples prepared simultaneously, one sample was intended for routine monitoring of the superconducting and microstructural properties of the TiN films, while the remaining three samples were intended for the preparation of nJJs and nanoSQUIDs.

The microstructures of the multilayers and devices on buffered Si substrates were studied by HRSEM using a Zeiss 1550 VP microscope and HRTEM using an FEI Tecnai G2 F20 microscope. A Quantum Design DynaCool system and a Physical Property Measurement System (PPMS) were used to measure the temperature dependence and magnetic field dependence of the nJJ and nanoSQUID resistances down to a temperature of 1.9 K. Measurements of CVCs of the nJJs at lower temperatures down to  $\sim 10$  mK were performed using a dilution refrigerator (Oxford Instruments Triton 400). Noise spectrum measurements of the nanoSQUIDs were performed using home-made nanoSQUID control electronics and an Agilent 35670A dynamic signal analyzer.

The noise spectrum was measured at the output of the measurement system, which consists of low noise room temperature electronics with a gain of 10 000 direct-coupled without signal modulation to the nanoSQUID immersed in liquid helium at 4.2 K. No magnetic shielding was used. The magnetic flux through the nanoSQUID loop was biased to the optimal operation point  $0.25 \Phi_0$  or an effective bias magnetic field of  $B = 1.5$  mT by the direct injection of a current of  $\sim 2$  mA into the nanoSQUID's loop using the third electrode. This

current flows between the electrodes on the right side of the nanoSQUID, which is shown in figure 6.

### 3. Experimental results

The deposited TiN films were optically mirror-like and golden in color. They demonstrated excellent corrosion resistance: their optical and electrical properties were unchanged even after keeping the films for over one month in the AZ<sup>®</sup>726 MIF developer. This is an important technological advantage over commonly-used elemental superconductors such as Nb and Al. When using the same developer and similar film thicknesses, Nb films were dissolved in a few hours and Al films in only 2 min, resulting in stronger technological restrictions on the patterning of Nb and Al films when compared with TiN films. For the fabrication of nanobridges, in particular, it is essential that Al and Nb produce oxide layers rapidly on their surface by natural oxidation in air at 1 bar and room temperature [35]. The thickness of a Nb oxide layer is  $\sim 10$  nm, which is comparable to the coherence length in Nb films of  $\sim 10$  nm and to the optimal thickness of the nanobridges. The high corrosion resistance of TiN films guarantees the long-term stability of thin film TiN-based devices.

Figure 1 shows a cross-sectional HRTEM image of a SiN-buffered Si substrate with a TiN film viewed along the [110] crystallographic direction of Si. The image shows primarily (200)-oriented growth of the columnar polycrystalline TiN film and an amorphous structure of the SiN buffer layer (see figure 1(b)). The columns in the TiN film have sizes of 20–30 nm in the plane parallel to the substrate surface. They propagate in the normal direction through the entire thickness of the film. The in-plane cross-sectional size of the crystallites and their orientation remain constant through the film thickness. The grains are misoriented in the plane parallel to the substrate surface (the *ab* plane), which may be a consequence of stress relaxation during film growth.

The LPCVD-grown 40 nm thick SiN buffer layers are pore-free and can be used as hard masks for wet chemical etching of single crystalline Si substrates by KOH solution in water for the local thinning of Si wafers or for the creation of free-standing SiN membranes that can be used for HRTEM [36]. The etch rate along the [001] crystallographic direction of Si in a 20% KOH solution at 80 °C is  $\sim 40 \mu\text{m h}^{-1}$  (see figure 2).

Wet etching in KOH solution may serve as an alternative method to the 300 W inductively coupled plasma (ICP) RIE of the Si substrates in pure SF<sub>6</sub> gas that was demonstrated for the preparation of nanoSQUID cantilevers [8]. In the case of ICP RIE thinning of Si substrates, the plasma etching is isotropic, with a large undercut that leads to a relatively large thinned area of approximately 5 mm  $\times$  5 mm. The thinned area has a typical thickness of  $\sim 60 \mu\text{m}$ , which makes it so flexible that it bends under vacuum during spin coating of the e-beam resist. The wet etching is anisotropic and allows for the fabrication of finer deep trenches in Si directly under a particular nanoSQUID to improve the homogeneity of the temperature distribution during the deposition of TiN films and to avoid bending of the substrate under vacuum during spin coating of

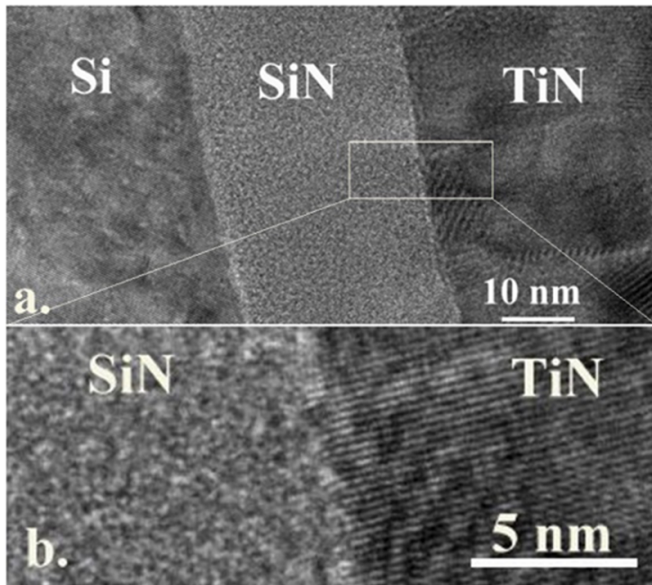


**Figure 1.** HRTEM image showing a TiN film deposited on a SiN-buffered Si (100) substrate: (a) overview of the Si–SiN–TiN heterostructure; (b) magnified view of the SiN–TiN interface.

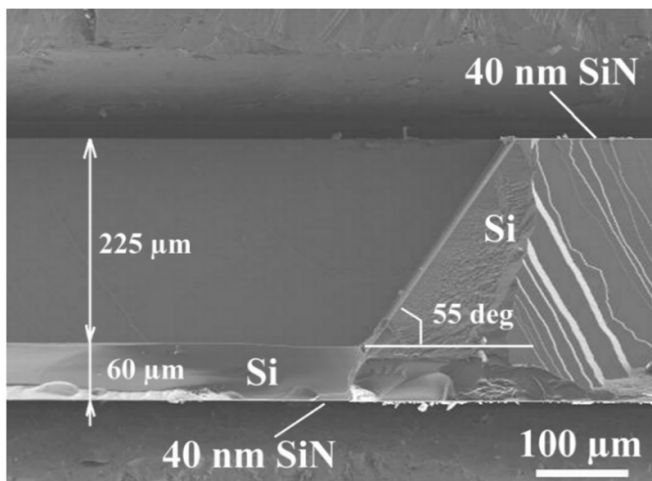


**Figure 2.** SEM image of a cross-section of a 285  $\mu\text{m}$  thick Si substrate after 5.5 h of etching in 20% KOH solution at 80  $^{\circ}\text{C}$  using a double-sided hard mask of 40 nm thick LPCVD-grown SiN.

the e-beam resist. The front side of the Si wafer was kept outside the KOH solution to prevent its degradation during wet etching.

The SiN buffer layer also serves as a stop layer for RIE of the TiN film. Without a SiN buffer layer, RIE proceeds into the intrinsic Si substrate with an etching rate that is  $\sim 15$  times faster than the RIE rate for TiN films, which is  $\sim 1 \text{ nm s}^{-1}$  under the same  $\text{SF}_6$  plasma conditions.

Figure 3 shows the temperature dependence of the resistivity of a 100 nm thick TiN film. Values of resistivity of  $\sim 11 \mu\Omega \text{ cm}$  at room temperature and  $\sim 5.3 \mu\Omega \text{ cm}$  at 5 K were observed. These values correspond to those obtained for TiN films deposited on an oxide-free Si surface at 800  $^{\circ}\text{C}$  [24, 37]. The superconducting transition temperature  $T_c \cong 4.75 \text{ K}$  is

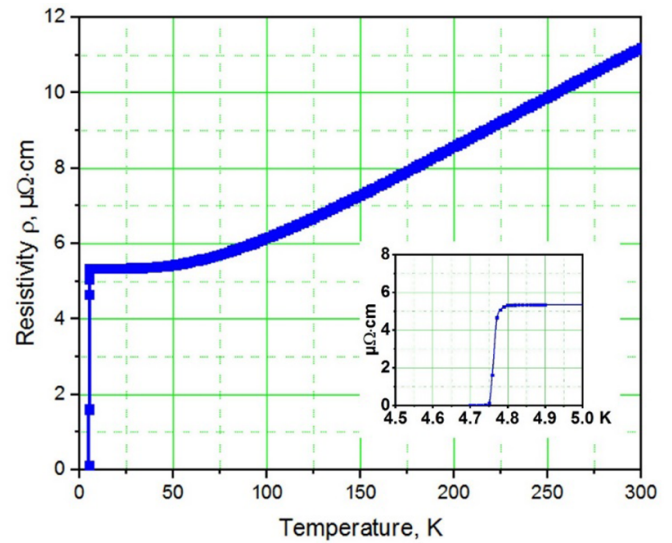


**Figure 3.**  $R(T)$  dependence of a 100 nm thick TiN film grown on a SiN-buffered Si substrate. The inset shows a detailed view near the superconducting transition temperature.

well suited to the operating temperature of 4.2 K of the nanoSQUIDS. The value of  $T_c$  depends on the thickness of the TiN films and is up to  $\sim 5.1 \text{ K}$  for 700 nm thick films [24]. It also has a strong dependence on sputtering conditions: base pressure, nitrogen partial pressure and substrate temperature [37]. The nitrogen partial pressure in the sputtering atmosphere influences  $T_c$  by changing the nitrogen content  $x$  in the  $\text{TiN}_x$  films. A partial pressure of nitrogen of more than 10% leads to a decrease of  $T_c$ , corresponding to values of  $x > 1$ . A relatively low base pressure of  $\leq 10^{-7}$  mbar, which is achieved in the chamber of the sputtering machine by using oil-free pumps and a higher substrate temperature of  $\geq 800 \text{ }^{\circ}\text{C}$ , is essential for achieving a relatively high value of  $T_c$  of the TiN films.

The residual resistance ratio (RRR)  $R_{300\text{K}}/R_{10\text{K}} \cong 2$  reflects a relatively long mean free path of charge carriers as a result of a low concentration of impurities and other crystallographic defects. Samples prepared (for comparison) on MgO substrates demonstrated much better epitaxial growth, with cube-on-cube-oriented practically single crystalline TiN films that have  $\sim 50\%$  lower resistivity and a higher RRR of  $R_{300\text{K}}/R_{10\text{K}} \cong 2.7$  for similar deposition conditions and thickness, probably corresponding to an even longer long mean free path of charge carriers. However, the TiN films that were grown on MgO substrates had worse superconducting properties, with  $T_c \cong 3.45 \text{ K}$ , which is too low for operation at 4.2 K. A lower resistivity in combination with a lower value of  $T_c$  are known for some other superconductors. For example, disorder resulting from the inclusion of O in Al increases its resistivity and doubles the  $T_c$  value of  $\text{AlO}_x$  from 1.2 K to 2.4 K, while a lower value of  $T_c$  for lower resistivity is observed in overdoped  $\text{YBa}_2\text{Cu}_3\text{O}_{7-x}$ , when compared with optimally doped  $\text{YBa}_2\text{Cu}_3\text{O}_{7-x}$  (see, for example [38]).

Low power (25 W) RIE of TiN films in  $\text{SF}_6$  gas at 5 Pa and 20  $^{\circ}\text{C}$  has demonstrated an etching rate of  $\sim 1 \text{ nm s}^{-1}$

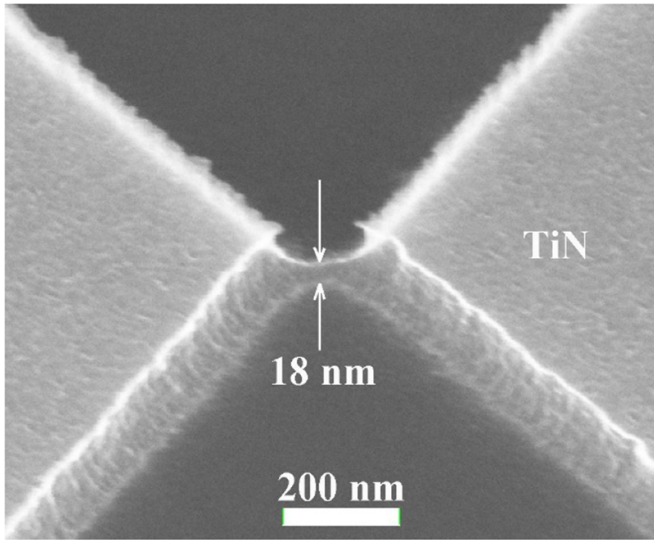


**Figure 4.** HRSEM image of an 18 nm wide TiN nJJ recorded at a 45° sample tilt angle. The mask of the diluted nLOF resist has been removed using acetone.

and a sufficiently good selectivity of  $\sim 3$  relative to the etching rate of the mask of a diluted nLOF 2020 resist. This selectivity is  $\sim 3$  times less than for hydrogen silsesquioxane (HSQ) electron beam resist [8, 24]. However, the nLOF resist has the advantage of a much longer shelf life, it requires  $\sim 20$  times lower dose for exposure by the electron beam and, after RIE, residuals of the nLOF resist can be removed using acetone and oxygen plasma. The etch rate increases with etch time due to an increase in substrate temperature during RIE. Contamination of the inner surface of the chamber of the RIE machine hinders etching. In order to achieve reproducibility of etching rates, sufficiently long ( $>30$  min) cleaning and preconditioning procedures were performed in the RIE machine before introducing the samples.

As a result of the isotropic etching behavior of TiN in  $\text{SF}_6$  plasma, undercutting occurs at an in-plane rate of  $\sim 0.3 \text{ nm s}^{-1}$ . The top of the film is then etched under the nanobridge of the resist mask, making the center of the TiN nanobridge thinner than the TiN film at the electrodes. In this way, a variable thickness nanobridge with a triangular cross section is created. The undercut can be reduced or even avoided by varying the RIE parameters. Figure 4 shows an HRSEM image of an 18 nm wide TiN variable thickness nJJ recorded at a 45° sample tilt angle. In this image, the mask of the diluted nLOF resist has already been removed.

The normal state resistivity  $T_c$  and the critical current density of the nJJs depend strongly on their cross-section. The temperature dependence of the normal state resistivity evolves from metallic to semiconducting and insulating behavior as the width of the nanobridge is reduced down to the sub-10 nm scale. This evolution is accompanied by a reduction in  $T_c$  and critical current density of the nJJs. TiN nJJs that have widths of  $<20$  nm are considered for operation in all-TiN qubits at temperatures of  $<20$  mK. Figure 5 shows CVCs of an 18 nm wide low- $I_c$  nJJ measured at temperatures down to  $\sim 10$  mK.

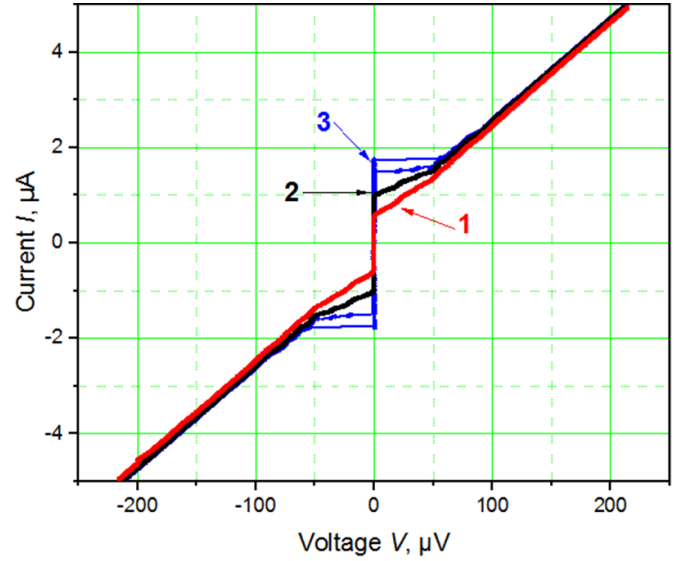


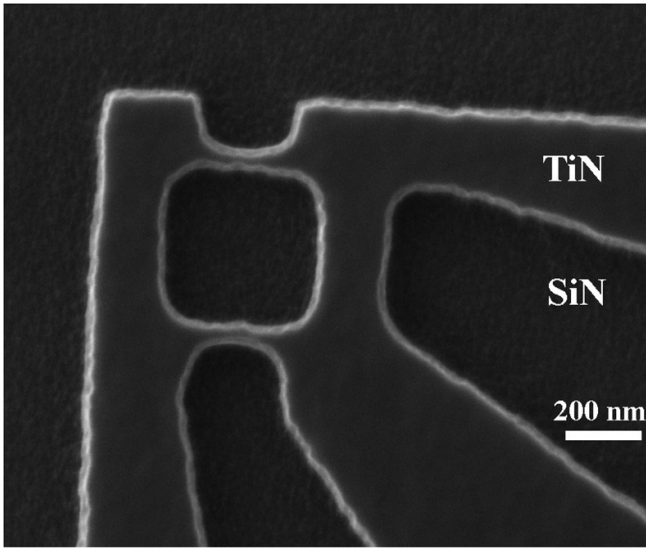
**Figure 5.**  $I(V)$  characteristics of an 18 nm wide TiN nJJ measured for both directions of swiping bias current at temperatures of 1.7 K (1-red), 1.2 K (2-black) and  $\sim 10$  mK (3-blue).

Critical currents of  $I_c(9 \text{ mK}) \cong 1.7 \mu\text{A}$ ,  $I_c(1.2 \text{ K}) \cong 1 \mu\text{A}$  and  $I_c(1.7 \text{ K}) \cong 0.5 \mu\text{A}$  were observed. These values fit well to theoretical predictions for nanobridges of ‘dirty superconductors’ [39], which are characterized by a charge carrier mean free path that is much shorter than the superconducting coherence length  $\xi_0$  in this material.

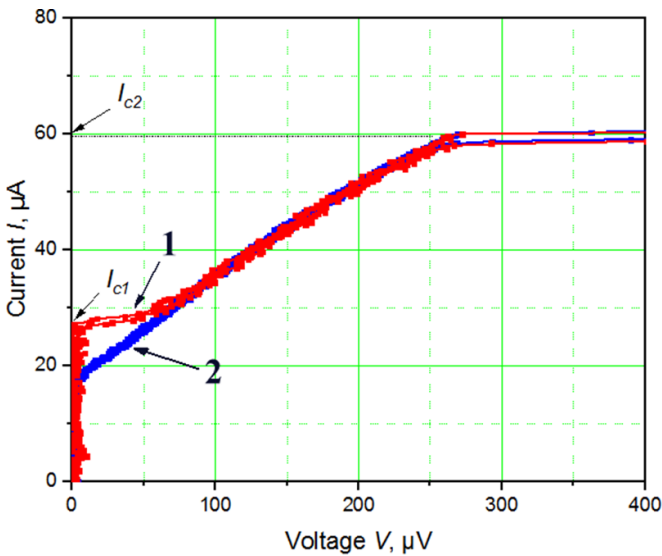
At  $\sim 10$  mK, the critical current is saturated and corresponds to the zero temperature critical current density  $J_c(0 \text{ K})$  of  $\sim 2 \text{ MA cm}^{-2}$ . For comparison, 30 nm wide nJJs that have relatively high critical currents (high- $I_c$ ) and are used for nanoSQUIDs demonstrate a critical current density of  $\sim 1 \text{ MA cm}^{-2}$  at an operating temperature of 4.2 K.

Figure 6 shows an HRSEM image of a TiN nanoSQUID with 30 nm wide nJJs prepared using RIE on an LPCVD SiN-buffered Si substrate. Such nJJs have a superconducting transition temperature  $T_c \cong 4.5 \text{ K}$ . The mask of the diluted nLOF resist has been removed using acetone. By the injection of current into a part of the loop of the nanoSQUID through an additional electrode, it is possible to bias the magnetic flux through the loop [8, 16, 24]. The estimated magnetic geometrical inductance of the  $200 \text{ nm} \times 500 \text{ nm}$  stripe in the loop of the nanoSQUID is  $L_g \cong 0.175 \text{ pH}$ . The critical current of this stripe  $I_c \cong 3 \text{ mA}$  corresponds to a critical current density of  $15 \text{ MA cm}^{-2}$  and produces the magnetic flux bias of  $\geq 0.25 \Phi_0$  through the loop of the nanoSQUID that is required for optimal nanoSQUID operation.

$I(V)$  curves of the optimized all-TiN high- $J_c$  nJJs are non-hysteretic at 4.2 K. Figure 7 shows the CVCs of a TiN nanoSQUID with 30 nm wide nJJs measured in magnetic fields of 0 mT (red) and 3 mT (blue) at 4.2 K. Just as in [14], two critical currents are observed. The smallest one at a bias current of  $I_{c1} \cong 27 \mu\text{A}$  is related to a transition between the zero voltage state and the non-zero voltage state of two superconducting nJJs connected in parallel in the loop of the nanoSQUID. The higher critical current  $I_{c2} \cong 60 \mu\text{A}$



**Figure 6.** HRSEM image of a TiN nanoSQUID with 30 nm wide nJJs prepared using RIE on an LPCVD SiN-buffered Si substrate. The mask of the diluted nLOF resist has been removed using acetone.



**Figure 7.**  $I(V)$  characteristics of a TiN nanoSQUID with 30 nm wide nJJs recorded in 0 mT (1-red) and 3 mT (2-blue) magnetic fields at 4.2 K. Two critical currents  $I_{c1}$  and  $I_{c2}$  are observed.

corresponds to a final transition of the normal state of the nJJs and superconducting electrodes in the vicinity of the nJJs due to Joule heating with power  $P_J = IV$  over the superconducting transition temperature  $T_c$  of the TiN film. This critical current  $I_{c2}$  often shows overheating hysteresis and does not depend on magnetic field on a mT scale. The slope  $R_n = dI/dV$  between  $I_{c1}$  and  $I_{c2}$  corresponds to the normal state resistance of TiN nJJs calculated using the resistivity value for the TiN film  $\rho(5 \text{ K}) \cong 5.3 \mu\Omega \text{ cm}$  obtained from figure 3.

The critical current  $I_{c1}$  is modulated periodically with a period of  $\sim 6$  mT by the magnetic field of the superconducting solenoid of the PPMS. The critical current  $I_{c2}$  does not

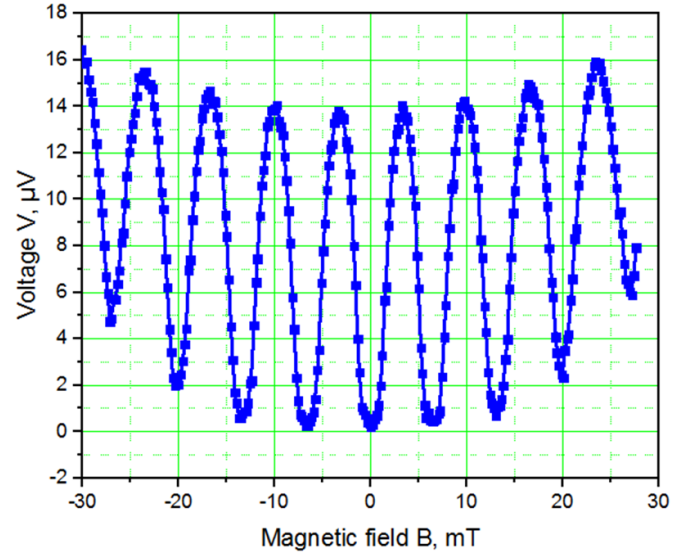


**Figure 8.** Voltage modulation  $V(B)$  of the nanoSQUID with 30 nm wide nJJs measured using a PPMS for a bias current of  $I_{c1} \cong 27 \mu\text{A}$  at 4.2 K.

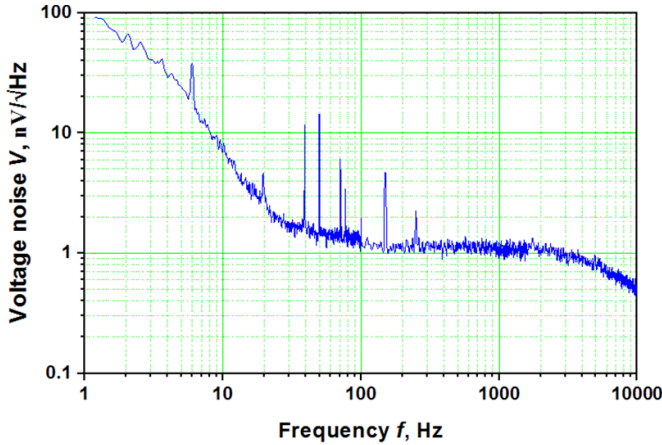
show a periodic modulation and decreases monotonically with increasing magnetic field of the solenoid over a larger scale of magnetic field of  $\sim 100$  mT.

Figure 8 shows the voltage modulation  $V(B)$  dependence of the nanoSQUID measured using a PPMS for a bias current of  $I_{c1} \cong 27 \mu\text{A}$  at 4.2 K. The peak-to-peak amplitude of the voltage modulations is  $\Delta V_{pp} \sim 14 \mu\text{V}$ , which corresponds to the maximal voltage response on magnetic flux  $\partial V/\partial \Phi \cong \pi \Delta V_{pp} \cong 44 \mu\text{V}/\Phi_0$ . The effective area and period of critical current modulation on magnetic field are  $\sigma_{\text{eff}} \cong 0.36 \mu\text{m}^2$  and  $\Delta B \cong 6$  mT, respectively [8, 16, 24]. More than 20 oscillations of the  $V(B)$  dependence with a period of  $\sim 6$  mT are observed. The increase in the voltage background value at higher magnetic fields is connected with the suppression of the critical currents  $I_c$  in the nJJs of the nanoSQUID.

Figure 9 shows the voltage noise spectrum recalculated to the input of the measurement system. The measurements were performed in ‘open loop’ mode without applying a feedback magnetic flux signal to the nanoSQUID loop. The noise level is determined primarily by the input white noise level  $\sim 1 \text{ nV}/\sqrt{\text{Hz}}$  of the room temperature preamplifier of the nanoSQUID’s control electronics and environmental noise, which is typical for magnetically-unshielded laboratory conditions.

#### 4. Discussion

Si substrates buffered by LPCVD SiN are well suited for the preparation of TiN nJJs and nanoSQUIDs with TiN nJJs operating at 4.2 K, despite the amorphous crystal structure of the LPCVD SiN. The  $T_c$  value of 100 nm thick TiN films on Si and SiN-buffered Si substrates is  $\sim 1$  K higher than the  $T_c$  value of epitaxial single-crystalline cube-on-cube-oriented 100 nm thick TiN films grown on (001) MgO substrates. The contamination of TiN films by different impurities segregated from



**Figure 9.** Voltage noise recalculated to the input of the measuring system, which uses a nanoSQUID immersed in liquid helium at 4.2 K. The noise is determined primarily by the noise of the room temperature preamplifier and the environmental magnetic noise detected by the nanoSQUID.

MgO substrates has a greater negative effect on  $T_c$ , when compared with the loss of epitaxial growth on an amorphous SiN buffer layer. Ca is one of the main impurities in MgO single crystals and is segregated at the elevated deposition temperature of  $\sim 800^\circ\text{C}$  [40]. Mitigation of the diffusion of impurities from MgO substrates by the introduction of a SrTiO<sub>3</sub> blocking buffer layer has improved the superconducting properties of YBa<sub>2</sub>Cu<sub>3</sub>O<sub>7-x</sub> films [41, 42]. Si and SiN do not contaminate TiN films as strongly as is the case for MgO substrates and, in combination with a low base pressure and a high deposition temperature, result in better superconducting parameters of the TiN films.

The patterning of nJJs from TiN films is much easier than the patterning of Nb, NbN or NbTiN films, as a result of the  $\sim 10$  times larger coherence length and excellent corrosion resistance of the TiN films. Instead of using expensive, often unavailable and insensitive HSQ negative e-beam resist, which also has a relatively short shelf life, nanostructures can be written on much larger areas using cheaper and more sensitive AZ<sup>®</sup>nLOF 2020 negative e-beam resist (which is also easier to handle) diluted by AZ<sup>®</sup>ERB solvent down to a thickness of  $\sim 100$  nm. After nanopatterning, residuals of the nLOF resist can be removed using warm acetone in an ultrasonic bath, which does not degrade TiN films but does not work for HSQ.

Focused ion beam (FIB) milling also provides sufficient spatial resolution for the reproducible patterning of TiN nJJs. It can be used for small-scale superconducting circuits including nanoSQUIDs and nanomachining of cantilever tips. The implantation of Ga atoms during FIB milling is usually minimized by the use of sacrificial protective layers.

The superconducting transition temperature  $T_c \cong 4.5$  K of TiN nanobridges fits very well for their operation at 4.2 K as Josephson junctions within the framework of Ginzburg–Landau theory, making them a convenient and ultrasmall alternative to tunnel Josephson junctions in many circuits for superconducting electronics, including nanoSQUIDs. The superconducting coherence length in TiN

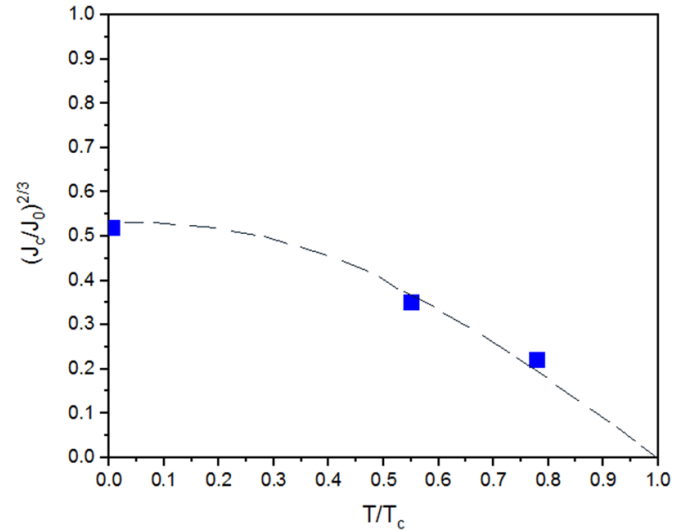


**Figure 10.** Normalized experimental values  $(J_c/J_0)^{2/3}$  plotted as a function of normalized temperature  $T/T_c$  derived from figure 5 using the fitting parameters  $J_0 = 4.8 \mu\text{A}$  and  $T_c = 2.1$  K, shown as blue squares. The theoretical dependence (dashed line) was calculated numerically in [39] for the case of dirty superconductors.

films  $\xi(4.2 \text{ K}) > 100$  nm [24] is much larger than the average grain size of 25 nm in the *ab* plane in the polycrystalline TiN films, suggesting that the grain boundaries do not degrade the superconducting properties. This situation can be compared with the case of high temperature superconductors such as YBa<sub>2</sub>Cu<sub>3</sub>O<sub>7-x</sub>, which have an in-plane coherence length of  $\sim 1.2$  nm at 4.2 K and  $\sim 4$  nm at 77 K, leading to weak link behavior of grain boundaries in these materials [43].

Figure 10 shows three experimental values of the temperature dependence of  $I_c$  derived from figure 5 for the nJJ shown in figure 4, together with a numerically-calculated theoretical estimate for dirty superconductors (see curve II in figure 2 in [39].) using the fitting parameters  $J_0 = 4.8 \mu\text{A}$  and  $T_c = 2.1$  K. Good agreement is obtained between the experimental values and theoretical estimations. The critical current is saturated at temperatures below  $\sim 0.6$  K, resembling the behavior of tunnel Josephson junctions. This is advantageous for applications of such nJJs at mK temperatures. Nevertheless, for applications in qubits, the critical current should be further reduced to  $I_c$  values of  $\sim 100$  nA. A reduction in critical current with a simultaneous increase of resistivity in the normal state can be achieved, for example, by increasing the nitrogen content in TiN<sub>x</sub> films, which are deposited at a higher partial pressure of nitrogen. In this case, the TiN<sub>x</sub> films will still be oxygen-free and described by the theory of dirty superconductors with a smaller value of the mean free path of the charge carriers.

The voltage on the nanoSQUID has a maximum response to magnetic field  $dV/dB$  at a  $0.25 \Phi_0$  magnetic flux bias, which corresponds to 1.5 mT for the nanoSQUID shown in figure 6. The geometrical inductance of the part of the nanoSQUID's loop between the right electrodes in figure 6 is already so small that a flux biasing current that approaches the depairing current in the TiN film is required. Smaller nanoSQUID loops can be flux biased using the Josephson inductances of additional

and wider nJJs, as in flux qubits [44]. The Josephson inductance  $L(\Delta\varphi) = \Phi_0/2\pi I_c \cos(\Delta\varphi)$ , where  $\Delta\varphi$  is the phase difference between the wave functions in the electrodes of wider nJJs, is derived from the potential Josephson energy instead of the energy of a magnetic field. We found that the Josephson inductance is more effective for direct current flux biasing of the nanoSQUID loop, when compared to the purely kinetic and/or geometric inductances of non-Josephson constrictions in thin superconducting films.

By using the voltage response to magnetic flux  $\partial V/\partial\Phi \cong 44 \mu\text{V}/\Phi_0$  and the effective area of the nanoSQUID  $(1/6) \Phi_0/m\text{T} \cong 0.345 \mu\text{m}^2 \cong (0.6 \mu\text{m})^2$ , we formally obtain for the present measurement system, which uses a TiN nanoSQUID operating at 4.2 K, a magnetic flux resolution  $\sqrt{S_\Phi} \cong 23 \mu\Phi_0/\sqrt{\text{Hz}}$ . This value is typical for a nanoSQUID measurement system with a room temperature preamplifier ( $\sqrt{S_\Phi} \cong 33 \mu\Phi_0/\sqrt{\text{Hz}}$  in [45]). Among planar nanoSQUIDs, flux noise values of  $0.3 \mu\Phi_0/\sqrt{\text{Hz}}$  [17] and  $1.7 \mu\Phi_0/\sqrt{\text{Hz}}$  [19] have been achieved. In both cases, the  $I(V)$  characteristics of the nanoSQUIDs were hysteretic. The goal of our paper is the realization and characterization of planar nanoSQUIDs that are non-hysteretic at 4.2 K. This property is necessary for applications, in which the output signal of the nanoSQUIDs should follow the measured magnetic flux continuously. In the present paper, the nanoSQUIDs were investigated close to  $T_c$  (4.2 K/4.5 K = 0.93) of the thin superconducting films and observed to be non-hysteretic, according to Ginzburg–Landau theory [25]. Close to  $T_c$ , the nanobridges are non-hysteretic and demonstrate ideal Josephson behavior [25]. However, the superconducting energy gap is smaller close to  $T_c$  than at lower temperature, which can explain the larger value of magnetic flux noise in the present paper and in [45].

The noise level of the nanoSQUID's measurement system is not equivalent to the intrinsic noise of the nanoSQUID that is implemented in this system and can be reduced by up to two orders of magnitude in future experiments by the implementation of a low- $T_c$  SQUID series array amplifier (SSA), similar to that demonstrated in [46] or a very large SSA of 800 high- $T_c$  SQUIDs operating at 77 K [47].

The resistively-shunted junction (RSJ) model can be applied to junctions made of nanobridges in the superconducting state at temperatures close to  $T_c$  (see, for example [25]). Moreover, according to [25], sufficiently small nanobridge Josephson junctions demonstrate the 'ideal' Josephson effect. As shown in [27, 48, 49], the superconducting current  $I_s$  through such a nanobridge, under this approximation, follows the ideal Josephson current-phase relationship  $I_s = I_c \sin(\phi)$ . It has been demonstrated experimentally [26] that at a temperature close to  $T_c$  the CVCs of Nb nJJs follow the RSJ model almost ideally. An advantage of TiN nJJs is that their typical  $T_c$  is within 10% above 4.2 K. At 4.2 K, Ginzburg–Landau theory is valid for 30 nm wide TiN nJJs because the superconducting coherence length in TiN films can be much larger than all three dimensions of the nanobridge.

One can consider a nanobridge junction as an intrinsically shunted junction like an SNS junction or a high- $T_c$  grain boundary junction, where the formation of Johnson–Nyquist noise due to dissipative quasiparticle currents occurs

within the junction, in contrast to tunnel junctions that use an externally-connected shunting resistor to reduce the MacCumber parameter of the junction. The CVCs of nJJs fit to the RSJ model better than the CVCs of resistively shunted tunnel junctions because of the absence of parasitic inductance of the connection between the junction and the shunting resistor in the case of nJJs.

The intrinsic noise of TiN nanoSQUIDs with nJJs operating at 4.2 K can be estimated from the Johnson current noise  $i_n$  of the nJJs by using a similar approach to that reported in [14]. At sufficiently high frequencies, the noise of each nJJ has a white spectrum at the level  $I_n = (4k_B T/R_N)^{1/2} \sim 4.8 \text{ pA}/\sqrt{\text{Hz}}$ , where  $T = 4.2 \text{ K}$  and  $R_N = 10 \Omega$  is the normal state resistance of the nJJs. The total current noise of the nanoSQUID is  $I_n = i_n \sqrt{2} \sim 6.8 \text{ pA}/\sqrt{\text{Hz}}$  and the voltage noise  $V_n = R_d I_n \sim 136 \text{ pV}/\sqrt{\text{Hz}}$ , where  $R_d \sim 20 \Omega$  is the differential resistance of the nanoSQUID at a bias current slightly above the critical current  $I_{c1} = 27 \mu\text{A}$ . The intrinsic flux noise of the nanoSQUID is  $\sqrt{S_\Phi} \cong V_n/(\partial V/\partial\Phi) \cong 3 \mu\Phi_0/\sqrt{\text{Hz}}$ , the magnetic field resolution  $B_n = (\partial B/\partial\Phi)\sqrt{S_\Phi} \cong 19 \text{ nT}/\sqrt{\text{Hz}}$  and the spin sensitivity  $\sqrt{S_n} = (r/r_e)\sqrt{S_\Phi} \cong 659 \mu_B/\sqrt{\text{Hz}}$ , where  $r_e = 2.82 \times 10^{-15} \text{ m}$  is the classical electron radius [50].

The flux noise and spin sensitivity can be improved by more than one order of magnitude by reducing the size of the loop of a nanoSQUID and by a reduction in temperature. The best flux noise  $\sqrt{S_\Phi} \cong 42 \text{ n}\Phi_0/\sqrt{\text{Hz}}$  and spin sensitivity  $\sqrt{S_n} = 0.29 \mu_B/\sqrt{\text{Hz}}$  were achieved for a Pb nanoSQUID with a 39 nm effective loop diameter using an SQUID-on-tip configuration and operating at 300 mK [7]. At this temperature, the critical currents of the Josephson junctions are too high and cause hysteretic behavior, but in high magnetic fields above 1.5 T the critical currents are sufficiently suppressed and the nanoSQUID was usable in a field of up to  $\sim 3 \text{ T}$ . At temperatures below 4.2 K, planar TiN nanoSQUIDs also demonstrate hysteretic  $I(V)$  characteristics and should have lower critical current fluctuations than at 4.2 K. However, we have not performed detailed investigations of the properties of hysteretic nanoSQUIDs in the present work.

## 5. Summary

We have fabricated TiN nJJs and nanoSQUIDs on Si substrates buffered by 40 nm thick LPCVD SiN films. HRTEM images of the TiN–SiN heterostructure reveal a columnar structure of the TiN film on an amorphous SiN buffer layer. Superior corrosion resistance, a large coherence length, a suitable superconducting transition temperature and high selectivity RIE of TiN relative to e-beam resists and the SiN buffer layer allow for reproducible preparation and result in long-term stability of the TiN nJJs. HRSEM images reveal the variable thickness shape of the nJJs. A combination of wet etching in 20% KOH and RIE was used for bulk nanomachining of nanoSQUID cantilevers. Non-hysteretic CVCs of the nJJs and nanoSQUIDs, as well as  $\sim 14 \mu\text{V}$  peak-to-peak voltage modulation on magnetic field  $V(B)$  of the nanoSQUIDs, were measured at 4.2 K. The observed noise level is determined primarily by the input white noise level  $\sim 1 \text{ nV}/\sqrt{\text{Hz}}$  of the room temperature preamplifier

of the nanoSQUID's control electronics. CVCs of the TiN nJJs follow theoretical predictions for dirty superconductors down to  $\sim 10$  mK. The critical current is saturated at temperatures below 0.6 K, resembling the behavior of tunnel Josephson junctions. This behavior is advantageous for applications of such nJJs at mK temperatures. Our findings pave the way for nanoSQUIDs and superconducting electronics based on TiN nJJs operating non-hysteretically at 4.2 K as well as for all-TiN qubits operating at sub-100 mK temperatures.

### Data availability statement

All data that support the findings of this study are included within the article (and any supplementary files).

### Acknowledgments

The authors gratefully acknowledge the possibility to perform parts of the work at ER-C-1, HNF, PGI-4/JCNS-2, PGI-5, PGI-7 and PGI-9 in Forschungszentrum Jülich GmbH. The authors also gratefully acknowledge L Kibkalo, L Risters, H Stumpf, M Nonn, S Trelenkamp, F Lentz, E Neumann, O Petravic, S Nandi, B Schmitz and G Potemkin for technical assistance.

### ORCID iDs

M I Faley  <https://orcid.org/0000-0003-2768-2796>  
 H Fiadziushkin  <https://orcid.org/0000-0002-0456-7480>  
 B Frohn  <https://orcid.org/0000-0002-1404-9230>  
 P Schüffelgen  <https://orcid.org/0000-0001-7977-7848>  
 R E Dunin-Borkowski  <https://orcid.org/0000-0001-8082-0647>

### References

- [1] Clarke J and Braginski A I (eds) 2004 *The SQUID Handbook Volume I Fundamentals and Technology of SQUIDs and SQUID Systems* (Weinheim: Wiley-VCH)
- [2] Kleiner R, Koelle D, Ludwig F and Clarke J 2004 Superconducting quantum interference devices: state of the art and applications *Proc. IEEE* **92** 1534
- [3] Clarke J and Braginski A I (eds) 2006 *The SQUID Handbook Volume II Applications of SQUIDs and SQUID Systems* (Weinheim: Wiley-VCH)
- [4] Fagaly R L 2006 Superconducting quantum interference device instruments and applications *Rev. Sci. Instrum.* **77** 101101
- [5] Seidel P (ed) 2015 *Applied Superconductivity: Handbook on Devices and Applications* vol 2 (New York: Wiley)
- [6] Granata C and Vettoliere A 2016 Nano superconducting quantum interference device: a powerful tool for nanoscale investigations *Phys. Rep.* **614** 1
- [7] Anahory Y et al 2020 SQUID-on-tip with single-electron spin sensitivity for high-field and ultra-low temperature nanomagnetic imaging *Nanoscale* **12** 3174
- [8] Faley M I, Bikulov T, Bosboom V, Golubov A A and Dunin-Borkowski R E 2021 Bulk nanomachining of cantilevers with Nb nanoSQUIDs based on nanobridge Josephson junctions *Supercond. Sci. Technol.* **34** 035014
- [9] Barman A, Mondal S, Sahoo S and De A 2020 Magnetization dynamics of nanoscale magnetic materials: A perspective *J. Appl. Phys.* **128** 170901
- [10] Matlashov A, Schmelz M, Zakosarenko V, Stolz R and Semertzidis Y K 2018 SQUID amplifiers for axion search experiments *Cryogenics* **91** 125
- [11] Troeman A G P, van der Ploeg S H W, Il'ichev E, Meyer H-G, Golubov A A, Kupriyanov M Y and Hilgenkamp H 2008 Temperature dependence measurements of the supercurrent-phase relationship in niobium nanobridges *Phys. Rev. B* **77** 024509
- [12] Schmelz M, Stolz R, Zakosarenko V, Anders S, Fritzsche L, Roth H and Meyer H-G 2012 Highly sensitive miniature SQUID magnetometer fabricated with cross-type Josephson tunnel junctions *Physica C* **478** 77
- [13] Il'in K, Rall D, Siegel M, Engel A, Schilling A, Semenov A and Huebers H-W 2010 Influence of thickness, width and temperature on critical current density of Nb thin film structures *Physica C* **470** 953
- [14] Voss R F, Laibowitz R B and Broers A N 1980 Niobium nanobridge dc SQUID *Appl. Phys. Lett.* **37** 656
- [15] Hao L, Macfarlane J C, Gallop J C, Romans E, Cox D, Hutson D and Chen J 2007 Spatial resolution assessment of nano-SQUIDs made by focused ion beam *IEEE Trans. Appl. Supercond.* **17** 742–5
- [16] Rodrigo R, Faley M I and Dunin-Borkowski R E 2020 NanoSQUIDs based on Nb nanobridges *J. Phys.: Conf. Ser.* **1559** 012011
- [17] Russo R, Esposito E, Crescitelli A, Di Gennaro E, Granata C, Vettoliere A, Cristiano R and Lisitskiy M 2017 NanoSQUIDs based on niobium nitride films *Supercond. Sci. Technol.* **30** 024009
- [18] Holzman I and Ivry Y 2019 On-chip integrable planar NbN nanoSQUID with broad temperature and magnetic-field operation range *AIP Adv.* **9** 105028
- [19] Shishkin A G, Skryabina O V, Gurtovoi V L, Dizhur S E, Faley M I, Golubov A A and Stolyarov V S 2020 Planar MoRe-based dc nanoSQUID *Supercond. Sci. Technol.* **33** 065005
- [20] Cho E Y, Ma M K, Huynh C, Pratt K, Paulson D N, Glyantsev V N, Dynes R C and Cybart S A 2015  $\text{YBa}_2\text{Cu}_3\text{O}_{7-\delta}$  superconducting quantum interference devices with metallic to insulating barriers written with a focused helium ion beam *Appl. Phys. Lett.* **106** 252601
- [21] Schwarz T, Wölbing R, Reiche C F, Müller B, Martínez-Pérez M J, Mühl T, Büchner B, Kleiner R and Koelle D 2015 Low-noise  $\text{YBa}_2\text{Cu}_3\text{O}_7$  nano-SQUIDs for performing magnetization-reversal measurements on magnetic nanoparticles *Phys. Rev. Appl.* **3** 044011
- [22] Trbaldo E, Arpaia R, Arzeo M, Andersson E, Golubev D, Lombardi F and Bauch T 2019 Transport and noise properties of YBCO nanowire based nanoSQUIDs *Supercond. Sci. Technol.* **32** 073001
- [23] Vijay R, Levenson-Falk E M, Slichter D H and Siddiqi I 2010 Approaching ideal weak link behavior with three dimensional aluminum nanobridges *Appl. Phys. Lett.* **96** 223112
- [24] Faley M I, Liu Y and Dunin-Borkowski R E 2021 Titanium nitride as a new prospective material for nanoSQUIDs and superconducting nanobridge electronics *Nanomaterials* **11** 466
- [25] Likharev K K 1979 Superconducting weak links *Rev. Mod. Phys.* **51** 101
- [26] Shelly C D, See P, Ireland J, Romans E J and Williams J M 2017 Weak link nanobridges as single flux quantum elements *Supercond. Sci. Technol.* **30** 095013

- [27] Tinkham M 1996 *Introduction to Superconductivity* 2nd edn (Philadelphia, PA: McGraw-Hill)
- [28] Vershinin N, Filonov K, Straumal B, Gust W, Wiener I, Rabkin E and Kazakeviche A 2000 Corrosion behavior of the protective and decorative TiN coatings on large area steel strips *Surf. Coat. Technol.* **125** 229
- [29] Vissers M R, Gao J, Wisbey D S, Hite D A, Tsuei C C, Corcoles A D, Steffen M and Pappas D P 2010 Low loss superconducting titanium nitride coplanar waveguide resonators *Appl. Phys. Lett.* **97** 232509
- [30] Sage J M, Bolkhovsky V, Oliver W D, Turek B and Welander P B 2011 Study of loss in superconducting coplanar waveguide resonators *J. Appl. Phys.* **109** 063915
- [31] Chang J B et al 2013 Improved superconducting qubit coherence using titanium nitride *Appl. Phys. Lett.* **103** 012602
- [32] Kim S et al 2021 Enhanced coherence of all-nitride superconducting qubits epitaxially grown on silicon substrate *Commun. Mater.* **2** 98
- [33] Wenner J et al 2011 Surface loss simulations of superconducting coplanar waveguide resonators *Appl. Phys. Lett.* **99** 113513
- [34] Narayan J, Tiwari P, Chen X, Singh J, Chowdhury R and Zheleva T 1992 Epitaxial growth of TiN films on (100) silicon substrates by laser physical vapor deposition *Appl. Phys. Lett.* **61** 1290
- [35] Henry M D, Wolfley S, Monson T, Clark B G, Shaner E and Jarecki R 2014 Stress dependent oxidation of sputtered niobium and effects on superconductivity *J. Appl. Phys.* **115** 083903
- [36] Dwyer J R and Harb M 2017 Through a window, brightly: a review of selected nanofabricated thin-film platforms for spectroscopy, imaging, and detection *Appl. Spectrosc.* **71** 2051
- [37] Sun R, Makise K, Qiu W, Terai H and Wang W 2015 Fabrication of (200)-oriented TiN films on Si (100) substrates by DC magnetron sputtering *IEEE Trans. Appl. Supercond.* **25** 1101204
- [38] Faley M I, Poppe U, Soltner H, Dähne U, Klein N, Schultz H, Evers W and Urban K 1993 Variation of the oxygen content in YBa<sub>2</sub>Cu<sub>3</sub>O<sub>7</sub> films deposited by high oxygen pressure DC-sputtering *IEEE Trans. Appl. Supercond.* **3** 1082
- [39] Kupriyanov M Y and Lukichev V F 1980 Temperature dependence of pair-breaking current in superconductors *Sov. J. Low Temp. Phys.* **6** 210
- [40] Souda R, Dizava T, Ishezava Y and Oshima C 1990 Segregation of Ca ions at the MgO(001) surface studied by neutral beam incidence ion scattering spectroscopy *J. Vac. Sci. Technol. A* **8** 3218
- [41] Faley M I Reproducible step-edge Josephson junction *Patent US 9666783 B2 (granted 30.05.2017), Patent DE102012006825 B4 (granted 26. 02.2015), CN 104350623 B (granted 22. 02.2017), AU 2013243054 B2 (granted 23. 06.2016), and Patent EP 2834860 B1 (granted 30. 12.2015)*
- [42] Faley M I, Dammers J, Maslennikov Y V, Schneiderman J F, Winkler D, Koshelets V P, Shah N J and Dunin-Borkowski R E 2017 High-T<sub>c</sub> SQUID biomagnetometers *Supercond. Sci. Technol.* **30** 083001
- [43] Hilgenkamp H and Mannhart J 2002 Grain boundaries in high-T<sub>c</sub> superconductors *Rev. Mod. Phys.* **74** 485
- [44] Chiorescu I, Nakamura Y, Marmans C and Mooij J 2003 Coherent quantum dynamics of a superconducting flux qubit *Science* **229** 1869
- [45] Lam S K H 2006 Noise properties of SQUIDs made from nanobridges *Supercond. Sci. Technol.* **19** 963
- [46] Hao L, Macfarlane J C, Gallop J C, Cox D, Beyer J, Drung D and Schurig T 2008 Measurement and noise performance of nano-superconducting-quantum interference devices fabricated by focused ion beam *Appl. Phys. Lett.* **92** 192507
- [47] Chesca B, John D and Cantor R 2021 SQUID-arrays coupled to on-chip integrated thin-film superconducting input coils operating coherently *Appl. Phys. Lett.* **118** 042601
- [48] Aslamazov L G and Larkin A I 1968 Josephson effect in superconducting point contacts *Pis'ma Zh. Eksp. Teor. Fiz.* **9** 88
- [49] Schmidt V V 1997 *The Physics of Superconductors* ed P Müller and A V Ustinov (Berlin: Springer)
- [50] Ketchen M B, Awschalom D D, Gallagher W J, Kleinsasser A W, Sandstrom R L, Rozen J R and Bumble B 1989 Design, fabrication, and performance of integrated miniature SQUID susceptometers *IEEE Trans. Magn.* **25** 1212–5